



HAL
open science

Induced microseismicity and tremor signatures illuminate different slip behaviors in a natural shale fault reactivated by a fluid pressure stimulation (Mont Terri)

Louis de Barros, Yves Guglielmi, Frédéric Cappa, Christophe Nussbaum, Jens Birkholzer

► To cite this version:

Louis de Barros, Yves Guglielmi, Frédéric Cappa, Christophe Nussbaum, Jens Birkholzer. Induced microseismicity and tremor signatures illuminate different slip behaviors in a natural shale fault reactivated by a fluid pressure stimulation (Mont Terri). *Geophysical Journal International*, 2023, 235 (1), pp.531-541. 10.1093/gji/ggad231 . hal-04123975

HAL Id: hal-04123975

<https://hal.science/hal-04123975>

Submitted on 9 Jun 2023

HAL is a multi-disciplinary open access archive for the deposit and dissemination of scientific research documents, whether they are published or not. The documents may come from teaching and research institutions in France or abroad, or from public or private research centers.

L'archive ouverte pluridisciplinaire **HAL**, est destinée au dépôt et à la diffusion de documents scientifiques de niveau recherche, publiés ou non, émanant des établissements d'enseignement et de recherche français ou étrangers, des laboratoires publics ou privés.

Induced microseismicity and tremor signatures illuminate different slip behaviors in a natural shale fault reactivated by a fluid pressure stimulation (Mont Terri)

Louis De Barros¹, Yves Guglielmi², Frédéric Cappa^{1,3}, Christophe Nussbaum⁴ and Jens Birkholzer²

¹ Université Côte d'Azur, CNRS, Observatoire de la Côte d'Azur, IRD, Géoazur, France

² Energy Geosciences Division, Lawrence Berkeley National Laboratory, Berkeley, California, USA

³ Institut Universitaire de France, Paris

⁴ Federal Office of Topography, Swisstopo, St-Ursanne, Switzerland

Correspondence to: Louis De Barros (debarros@geoazur.unice.fr)

Key Words

Induced seismicity; Rheology and friction of fault zones; Fracture and flow; decameter-scale in-situ experiment, shale and clay-rich faults

Short title: Seismic responses of slip on a fluid-activated shale fault

Abstract

Fault slip induced by fluid perturbation in shale formations may only lead to as sparse seismicity. However, fault slip may strongly impact the integrity of shale formations that serve as caprocks for geological reservoirs holding buoyant fluids such as CO₂, natural gas, or hydrogen. A better understanding of the fluid reactivation processes of fault and the seismic triggering process is therefore critical for reservoir monitoring and fault stability. Here we analyze the seismic responses of a shale fault exposed to fluid pressurization during an *in situ* field-scale injection experiment at ~340 m depth in the Mont Terri underground research laboratory (Switzerland). Two main types of seismic signals are observed as the fault was activated and started to slowly slip. After an aseismic phase, we observed tremor signatures and an increase in noise amplitude, which were directly associated with the slowly propagating fault slip in response to fluid injection. These signatures were later followed by micro-earthquakes that seem to occur further away from the fluid-pressurized area. We interpret these micro-earthquakes to be triggered by stress perturbations from the main slip growth. These two classes of seismic responses therefore highlight two different processes. Tremors seem to be a more direct observation for the fluid-induced slip propagation than micro-earthquakes. Even hidden in the noise, they precede earthquake failures, thus providing a useful tool for monitoring fluid leakage activated by slow deformation on low permeable shale faults, with applications for sealing integrity of caprocks.

ORIGINAL UNEDITED MANUSCRIPT

1. Introduction

Shale and clay-rich materials are common in the Earth's subsurface. They are important to the exploitation of geological resources, as they may contain natural gas that can be extracted through hydraulic fracturing (Gandossi and Von Estorff, 2013). They also form suitable caprock formations for geological reservoirs holding buoyant fluids (Olabode et al., 2012). However, faults within shale materials have a very low permeability ($k < 1 \times 10^{-17} \text{ m}^2$) that can suddenly increase by several order of magnitudes in response to failures triggered by local over-pressure (Guglielmi et al., 2015b). Their reactivation in the reservoir caprock may then lead to a loss of sealing integrity with potential fluid leakages, which is specifically an issue for large-scale carbon dioxide (CO₂) geological storage (Guglielmi et al., 2021). Such concerns require that the hydromechanical behavior of faults during fluid injection in shales is monitored at adequate temporal and spatial resolution such that potential leakage pathways can be detected early.

Micro-seismicity is one of the few observations of dynamic subsurface processes. For example, it is often used to track fluid flow and fracture propagation during geological reservoir stimulation, as for instance in hydrofracturing treatments (Eyre et al., 2019; Kettlety et al., 2020; Maxwell et al., 2010). However, observations show that induced seismicity may only be a secondary response to fluid pressure increase, while fluid-induced deformation is mainly aseismic (Cappa et al., 2019; Cornet et al., 1998; De Barros et al., 2018; Guglielmi et al., 2015a). This is particularly true in shale materials. Indeed, their specific elastic and rate-strengthening frictional properties as observed in the laboratory (Fang et al., 2017; Orellana et al., 2018; Sarout et al., 2017) favor slow and aseismic slip, which explains why only a sparse seismic response is observed *in situ* (De Barros et al., 2016; Eyre et al., 2022, 2019; Zoback et al., 2012). Why deformation only sometimes emits seismic events is still an open question. Indeed, seismicity may be rather linked to stress concentration in zones away from the fluid pressurized area, to fracture density or damage, to frictional asperities or to variations of mineralogy than to the fluid-pressure diffusion itself (De Barros et al., 2016; Orellana et al., 2018; Wang et al., 2022).

In addition to micro-seismicity, tremor-like signals, also called Long Period Long Duration (LPLD) events, were observed during hydraulic fracturing in shale (Das and Zoback, 2013; Eaton et al., 2013; Kumar et al., 2017; Li et al., 2018). Their existence has however been questioned, as seismic signatures of regional earthquakes or travelling trains might have been ambiguously interpreted as

LPLD events (Caffagni et al., 2015; Li et al., 2018; Zecevic et al., 2016). Moreover, the source mechanism of such events, if caused by fluid injection, are still under debate. Comparing them to tremors in subduction areas (Obara et al., 2004), they are interpreted as seismic signatures of slow-slip events. In volcanic environments, tremors are likely emitted by the resonance of fluid-filled cavities (Julian, 1994), which might also apply in reservoirs where fractures are hydraulically opened (Tary et al., 2014). Finally, as these signals are emergent and of low amplitude, their waveforms may be buried in the background noise and go undetected (Frank, 2016; Hulbert et al., 2022; Rouet-Leduc et al., 2018). In this case, they might be identified through variations in the noise amplitude and frequency content.

In summary, the processes behind fault seismic responses to fluid perturbation in shale materials, and their suitability to monitor either deformation processes or fluid diffusion in low-permeability formations are still open questions. Here, we analyze the field data from a fluid injection experiment in a shale fault to investigate the interplay between fault activation and seismicity. The experiment was performed in the low-permeability Opalinus Clay formation of the Mont Terri Underground Research Laboratory (URL) in Switzerland (Thury and Bossart, 1999). This *in-situ* decameter-scale experiment aimed at reactivating secondary splay faults of a primary multi-kilometer fault. A multimodal monitoring network allowed simultaneous measurement of fluid pressure, flowrate, fault displacement and seismic emissions. In this article, we focus on the seismic responses associated with the coupled hydromechanical processes that were previously analyzed (Guglielmi et al., 2021, 2020, 2017; Jeanne et al., 2018). After presenting the general context of the experiment, we analyze seismic events and noise variations in the light of the fluid pressure and deformation in the fault zone.

2. Experimental set-up

From a horizontal gallery, three vertical boreholes (Fig. 1) were drilled and are dedicated to (1) the injection (injection borehole), (2) the hydromechanical monitoring (monitoring borehole) and (3) the seismic monitoring (seismic borehole). The experiment is set in the hanging wall of the N50°, dipping 60°SE fault zone (Main Fault). This ~3 m wide thrust-fault zone is composed of lenses of scaly clay, intercalated within a network of secondary faults (Laurich et al., 2017; Nussbaum et al., 2011). In the injection borehole, the 2.4 m long chamber of the injection probe (called SIMFIP; Guglielmi et al., 2020) was centered at 40.6 m depth below the gallery floor (equivalent to ~340m below topographic

surface) on satellite splay faults about 2 m above the Main Fault. It was intersected by subparallel fault planes striking N040-to-N050° and dipping 35-to-55° SE, around which a 3D displacement sensor was anchored. These fault planes crosscut a second borehole (monitoring borehole, Fig. 1) located 3.1 m northwest of the injection at a depth of 37.65 m below the gallery floor. There, a second SIMFIP probe (later referred as “monitoring probe”), with another deformation sensor, was centered on a major N050°, dipping 61°SE, geological feature that delimits the top of the Main Fault zone (Guglielmi et al., 2020; Jeanne et al., 2018). In both SIMFIP probes, a Bragg optic fiber network allows the measure of the full strain tensor (Guglielmi et al., 2014), including dynamic signals up to 0.25 kHz. Fluid pressure is also monitored in those probes. A third borehole (seismic borehole, Fig. 1), located ~2 m north of the monitoring probe, was dedicated to seismic monitoring. Two sets of collocated sensors, composed of a vertical geophone, a 3C accelerometer and an acoustic sensor, were positioned 9 m apart, above and below the Main Fault zone. These seismic sensors have a flat response in the ranges 0.01-0.5 kHz, 0.01-4 kHz and 0.5-10 kHz, respectively. Therefore, this network of sensors allowed a continuous monitoring from the static deformation to the very high frequency seismic emissions.

Seismic events were first detected by a STA/LTA approach (Trnkoczy, 2009). However, because of a very high number of false detections (>500, mainly electrical glitches), we crosschecked the detected events and extended the catalog through interactive screening. We kept only the seismic signatures which are clearly seen on at least two different sensors (either collocated or not). Depending on the signal waveforms, we classified the events as either (1) micro-earthquakes if they showed a clear onset, identifiable P- and/or S-waves, and a short duration (<0.02 s on the accelerometers, which is the duration of the largest micro-earthquake we recorded), or (2) tremor-like signals, for emergent signatures with much longer duration (>0.1 s on the accelerometers). At the end, 53 events are kept as micro-earthquakes, and 5 time periods show tremor-type signatures. As tremor signatures are emergent with low amplitude, they may be buried in the noise. Therefore, we looked for possible hidden signals by characterizing the noise amplitude. To this aim, we used a band-pass filter on the dynamic signals recorded by the geophones (10-500Hz), accelerometers (0.1-2kHz) and strain sensors (2-240Hz). We then computed their squared amplitudes, related to the seismic energy, that we smoothed using a sliding median filter on a 2s long window. The cumulated energy shows a trend due to the presence of a continuous background and instrumental noise. We corrected it by removing the

mean trend computed during 2 minutes (17h25-17h27; Fig. 1) in the injection period but before the first failure in the injection chamber.

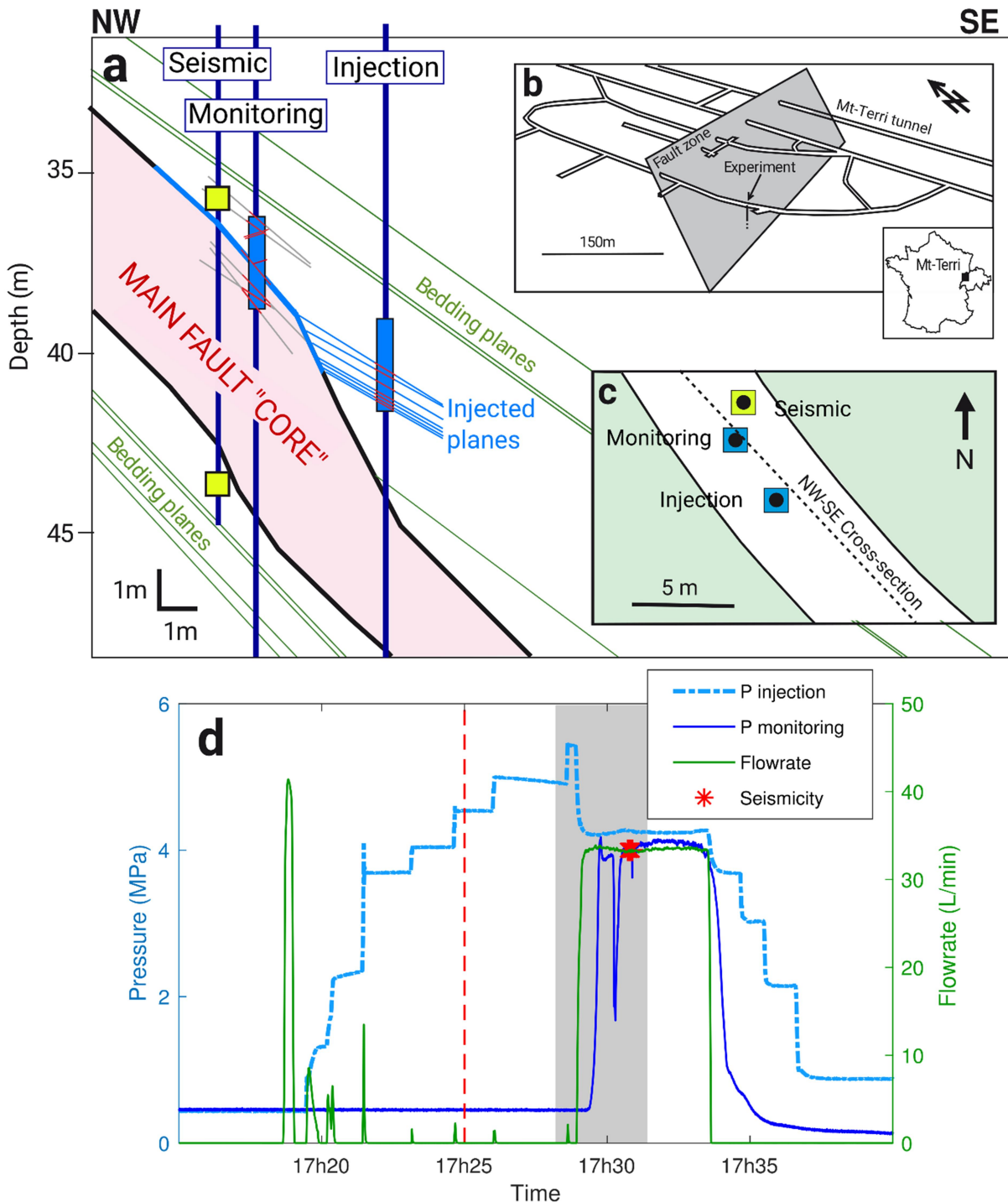


Figure 1. (a) Schematic NW-SE cross-section of the experimental set-up and its geological context. Geological features, highlighted in red in both chambers, are reconstructed from the borehole cores and image logs. The structures that were reactivated with fluid flow inside are shown in blue. The location within the Mont Terri URL and a map view showing the borehole positions are shown as inset in (b) and (c), respectively. (d) Flowrate

and fluid pressure measured in the injection and monitoring chambers. The red dashed line and the gray area show the reference time and the period used in Fig. 2.

3. General behaviors of the fault response to the injection

A first injection allowed the initiation of a fault slip at 3.5 MPa that was monitored by the deformation sensor of the injection probe (Guglielmi et al., 2020). Given the very limited injected volume (0.69 L), the slip did not propagate far from the injection and did not emit seismicity. However, it led to a ~10 fold increase of permeability (Jeanne et al., 2018). Then, a second injection phase, shown in Fig. 1d, propagated the fault slip from 17h19. The pressure was quickly increased up to 5.4 MPa causing the tested fault to slip and open at ~17h29 ($t=234s$, Fig. 2). A large (1.2 MPa) pressure drop from $P_{inj}=5.4$ MPa was recorded in the injection chamber, which triggered a sudden increase of the flowrate from nearly 0 to ~33 L/min and, later, a pressure increase up to 4.1 MPa in the monitoring chamber ($t=257s$, Fig. 2). Therefore, the triggered slip on the tested planes propagated from the injection up to the monitoring chamber. The time delay between fault shearing, opening and fluid pressure increase revealed the mixed-mode rupture process driving fluid propagation in low-permeability faults (Cappa et al., 2022). No seismic events were observed during this phase. During the next ~5 minutes (Fig. 1d), the pressure level stayed high in the monitoring chamber indicating a direct hydraulic connection between both chambers. A large pressure drop of more than 2 MPa ($t=313s$, Fig. 2) showed a first failure episode starting in the monitoring chamber. It was followed by a period of strong hydromechanical instability observed in the monitoring chamber, indicating several failure episodes (Fig. 2 and 3). On average, during this period, displacement was northward and westward, indicating the average horizontal direction of the slip propagation (Fig. 3). Given the fault orientation, this corresponds to a normal fault activation with a small right-lateral strike slip component. The large vertical displacements also suggested a strong opening component while slip was propagating (Guglielmi et al., 2020). Several bursts of micro-earthquakes and tremor signals were recorded during this stage (Fig. 3), on which we will focus in the next section. Finally, the injection pressure was artificially decreased step-by-step (Fig. 1d). For more details about the injection test, we refer the reader to Guglielmi et al. (2020).

In total, about 143 liters of water were injected without significant back-flow. Permanent residual displacements of 200 and 813 μm were observed at the injection and monitoring chambers,

respectively. The induced displacement at the injection and monitoring probes allows the determination of the stress state within the experiment zone (Guglielmi et al., 2020). It confirms the local stress state already determined by geological analysis in the Mont Terri laboratory (Martin and Lanyon, 2003), with a subvertical major stress component σ_1 of 6.2 MPa. The induced deformation is consistent with this stress state, but occurred at high value of injected pressure (5.4 MPa), which nearly reduced to zero the effective normal stress on the fault. Therefore, the injected fault was initially not in a critical state, which may explain the rupture with a strong opening component (Cappa et al., 2022; Guglielmi et al., 2020).

ORIGINAL UNEDITED MANUSCRIPT

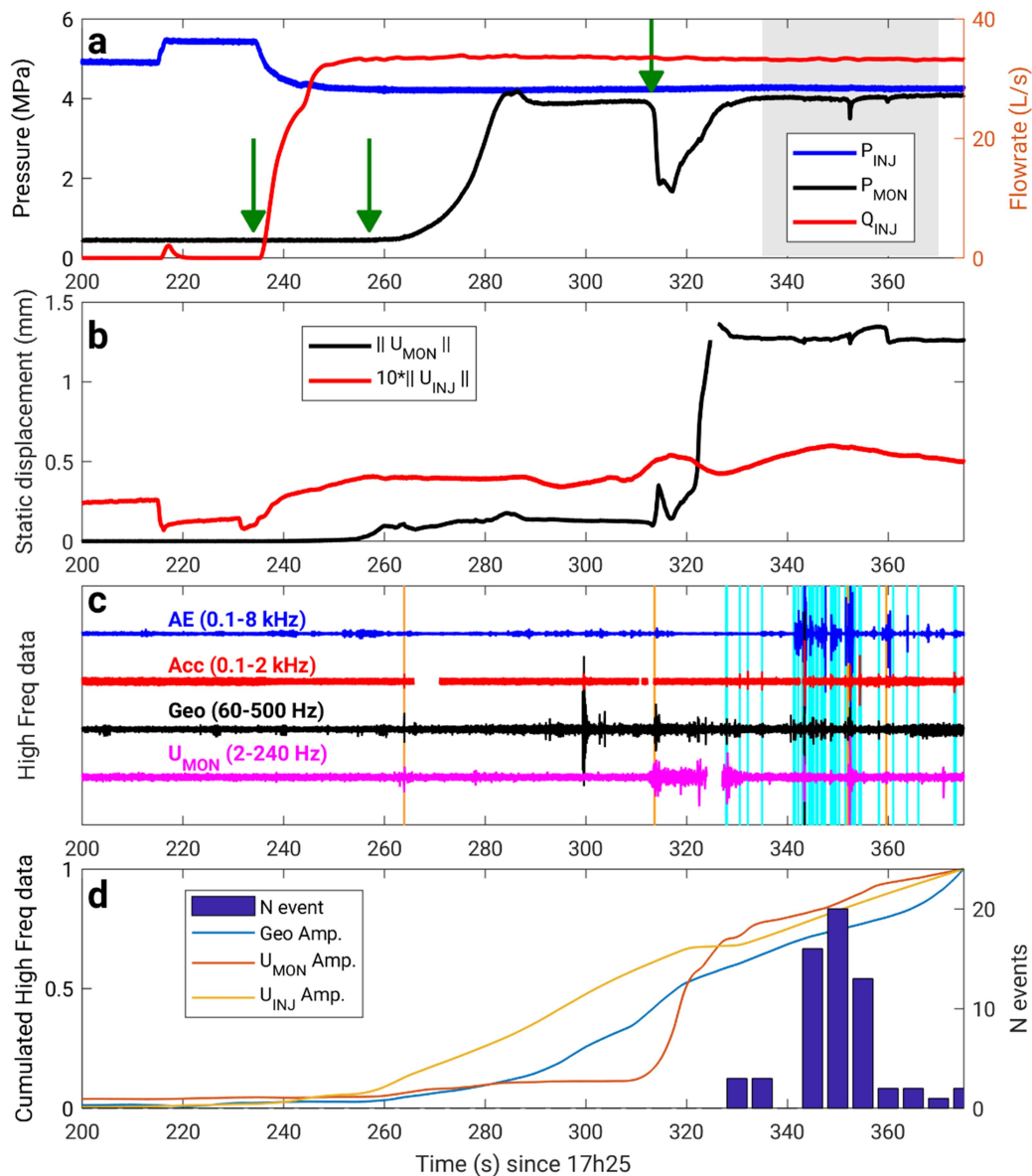


Figure 2. (a) Injected fluid pressure (P_{INJ}) and flowrate (Q_{INJ}) and monitored pressure (P_{MON}). Arrows highlight the start of the flowrate increase ($t=234s$), of the pressure increase ($t=257s$) and of the main failure episode ($t=313s$) in the monitoring chamber. The gray area shows the period on which Fig. 3 focuses. (b) Norm of the displacement at the injection ($10*U_{INJ}$ for visualization purpose) and monitoring (U_{MON}) probes. (c) Normalized dynamic signals recorded by the monitoring probe (U_{MON}), the upper geophone (Geo), accelerometer (Acc) and acoustic (AE) sensors, with their respective frequency range. The orange and cyan lines show the observed tremor-type signatures and micro-earthquakes, respectively. Data gaps correspond to instrumental issues. (d) Normalized cumulative dynamic data recorded by the injection and the monitoring probes (2-240 Hz) and the upper geophone (60-500 Hz). The histogram shows the distribution of the micro-earthquakes. The origin time is 17h25 (red line in Fig. 1).

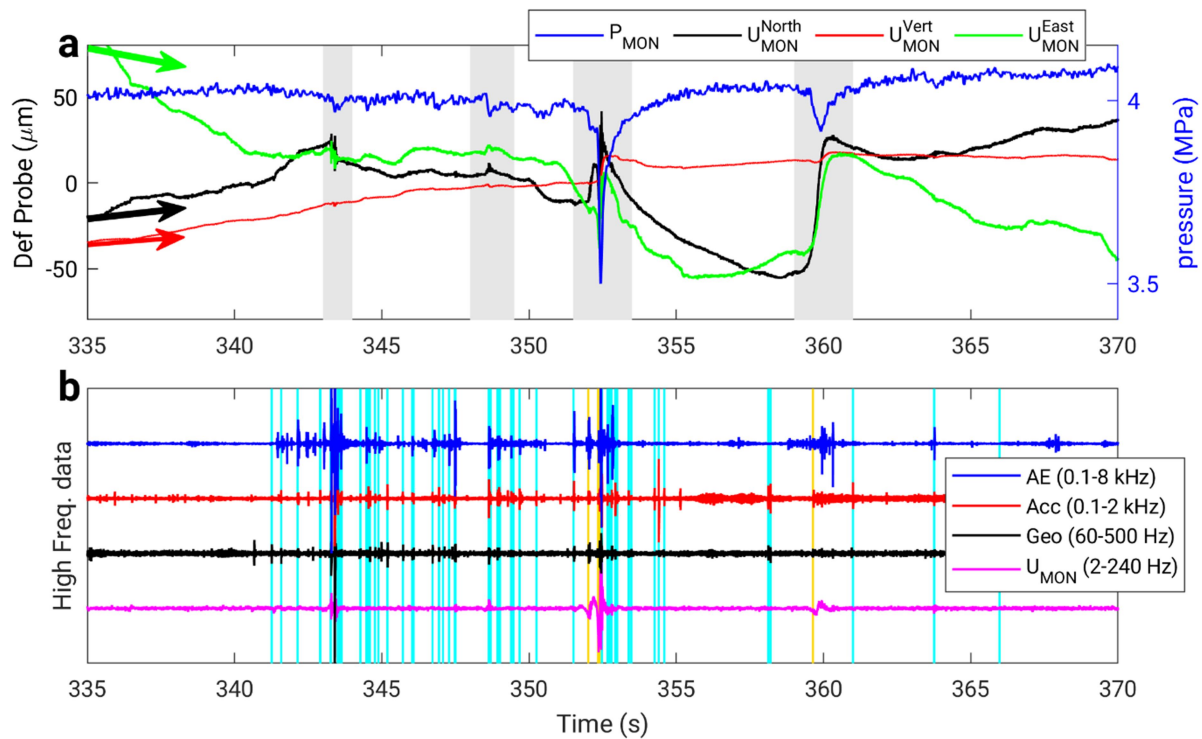


Figure 3. Close-up view on the period with seismic events of (a) the fluid pressure (right axis) and the 3 components (U_{MON}^{North} , U_{MON}^{Vert} and U_{MON}^{East}) of the deformation at the monitoring probe (Def Probe, left axis, in μm) and (b) the dynamic signals recorded by the monitoring probe (U_{MON}), the upper geophone (Geo) and accelerometer (Acc), and an acoustic sensor (AE), with their respective frequency range in the caption. In (a), the arrows highlight the main deformation direction and the gray areas show the seismic sequence periods on which Fig. 4 focuses. The yellow and cyan lines show the observed tremor-type signature and micro-earthquakes, respectively.

4. Seismic responses

4.1. Increase in background noise amplitude

The beginning of the test, including the first failures at the injection and the slip propagation between both probes, is devoid of micro-seismicity and seems totally aseismic. However, an interesting observation is that the cumulative high-frequency data increases while the slip propagates between the two probes (Fig. 2d). As no micro-earthquakes or tremor signals can be identified during this period, the cumulative data is caused by changes of amplitude of the signals that composed the noise. On the injection probe, this noise amplitude starts growing after the flow-rate increase and before the

hydraulic connection of both probes. On the monitoring probe, the noise increase is small when the pressure front is arriving ($t=257s$, Fig. 2), but sharpens during the first, large and aseismic failure ($t=313s$). The upper geophone data show amplitude change intermediate between these two behaviors, with an accelerating increase of the noise amplitude after the hydraulic connection between the probes. On this sensor, the noise amplitude increases mainly in the frequencies below 80 Hz and in the range 300-400 Hz (spectrogram in supplementary Fig. S1). No clear changes in the noise can be seen on the accelerometers, likely because these sensors are less sensitive to low frequency signals (Fig. S2 and S3).

This noise signature is clear on both the mechanical probes and the geophones, but with a different pattern. It could have been produced by external sources such as the pumping system. However, these sources are offset horizontally in the gallery by about 50 m from the borehole heads. They should produce similar pattern of amplitude changes on the different sensors, and particularly on the two geophones that are at close distance in the same borehole. Moreover, the seismic noise increases are delayed from the sharp increase of flowrate from nearly 0 to ~ 33 L/min, and it occurs in a period with constant pressure and flowrate at the injection. Therefore, even if the limited number of sensors does not allow a quantitative estimation of its origin, this transient change of amplitude is likely to have a local origin, as the near-field signature of a local transient.

ORIGINAL UNEDITED MANUSCRIPT

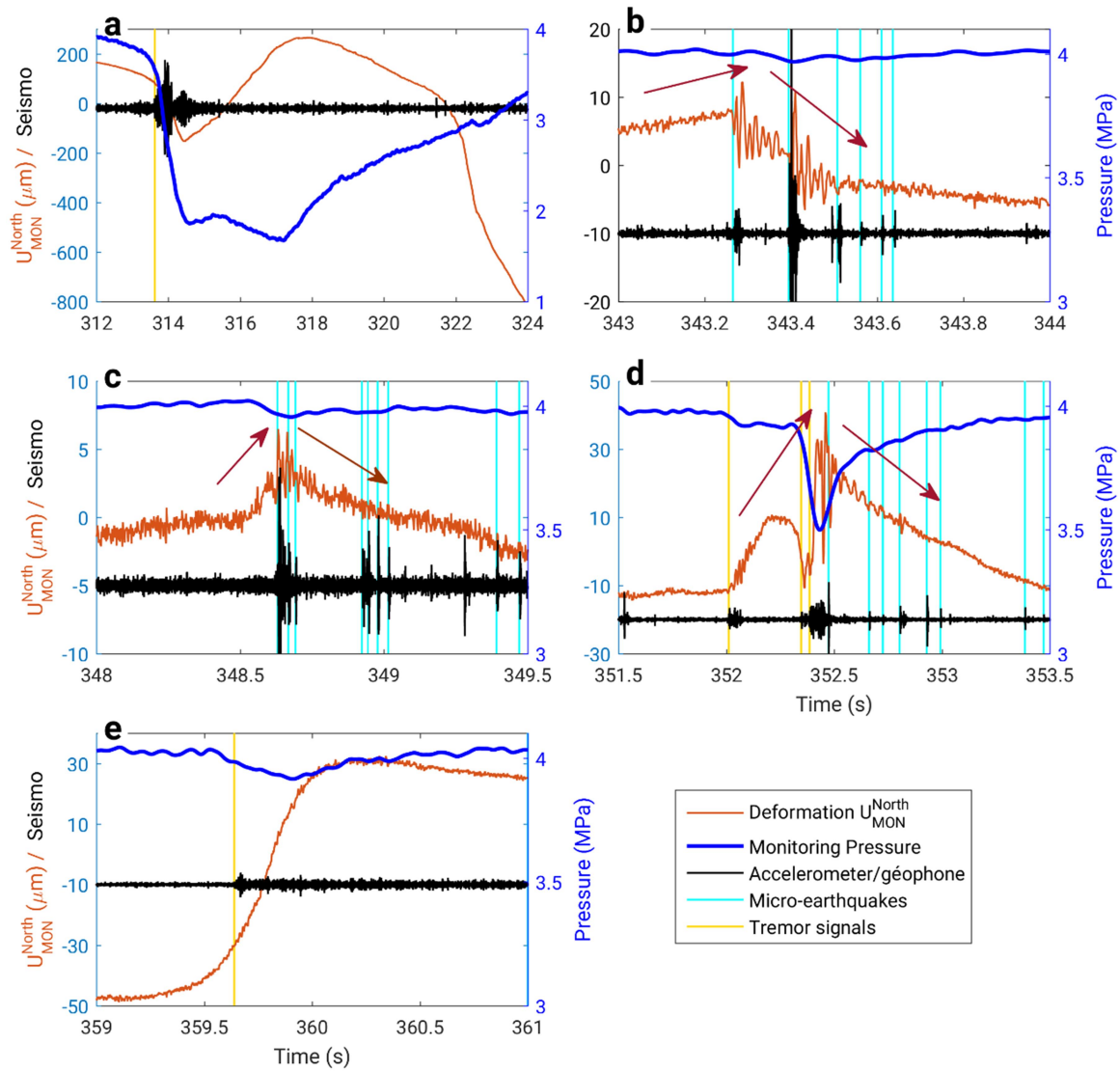


Figure 4. Close-up view on five seismic sequences (gray areas in Fig. 3), with fluid pressure and northward deformation measured by the monitoring probe. Seismic data are from the upper accelerometer (mm/s^2), except in (b) where the upper geophone data is shown (10^{-5} mm/s). Cyan and yellow vertical lines indicate micro-earthquakes and tremor signals, respectively. The brown arrows highlight the main deformation directions in the sequences (b), (c) and (d).

4.2. Tremor-type signatures

Clear signature of tremor-like signals can be identified, particularly when the pressure is at high level in the monitoring chamber. The first large fault failure observed at the monitoring point ($t=313\text{s}$), with a pressure drop of $\sim 2.1\text{ MPa}$, does not emit detected micro-earthquakes, but only a tremor-type signal, characterized by a duration longer than 1s, an emergent onset and spectral bands in the 0.05-0.3 kHz on the upper geophone (Fig. 4a and 5a). Because of this low-frequency content, this signal can be barely seen on the accelerometer (Supplementary Fig. S4).

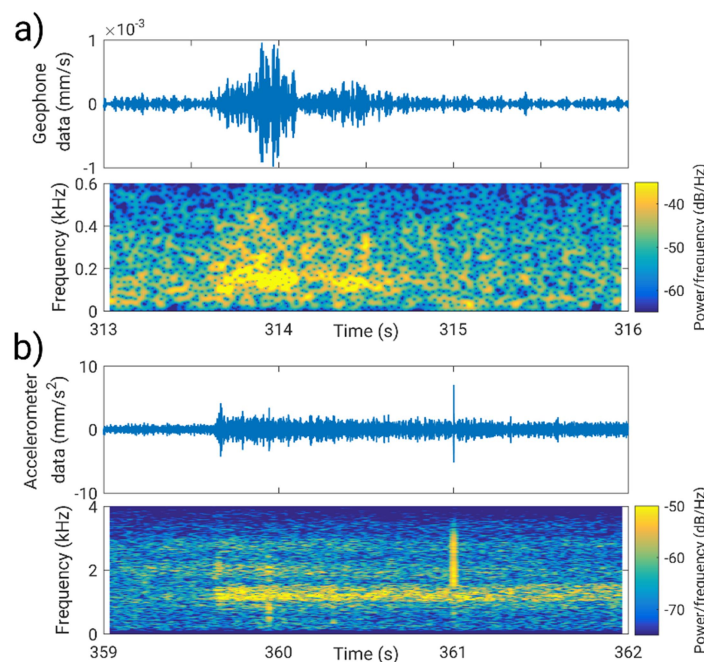


Figure 5. Tremor-like signals. (a) Upper geophone data and its spectrogram during the main first failure in the monitoring chamber ($t=313\text{-}316\text{s}$, Fig. 4a). (b) Upper accelerometer data and its spectrogram, in the $t=359\text{-}362\text{s}$ period (Fig. 4e).

Later, at $t=352\text{s}$, two successive decreases of pressure, the second one being of $\sim 0.5\text{ MPa}$, are both associated with tremor-like signals (Fig. 4d) of short duration (0.1s). They show a broad spectral content, which is however rich in low-frequency energy. These signatures can be seen on all types of sensors, including the mechanical probes (Supplementary Fig. S5). Between $t=359$ and 361s (Fig. 4e), a very large deformation with a small decay of pressure ($\sim 0.15\text{ MPa}$) is associated with a long-lasting ($\sim 4\text{s}$) tremor-like signature with a 0.8-1.5kHz high frequency content on the upper accelerometer (Fig.

5b). In both cases, these signals occurred within large deformation episode in the main fault slip direction.

4.3. Seismic burst sequences

Micro-earthquakes only occurred after the hydraulic connection between chambers and the main failure at the monitoring point ($t=313$ s). Only a few micro-earthquakes are detected during the next 30 s, before the occurrence of several bursts of events gathering a total of ~ 50 micro-earthquakes in the 340-370 s period (Fig. 3).

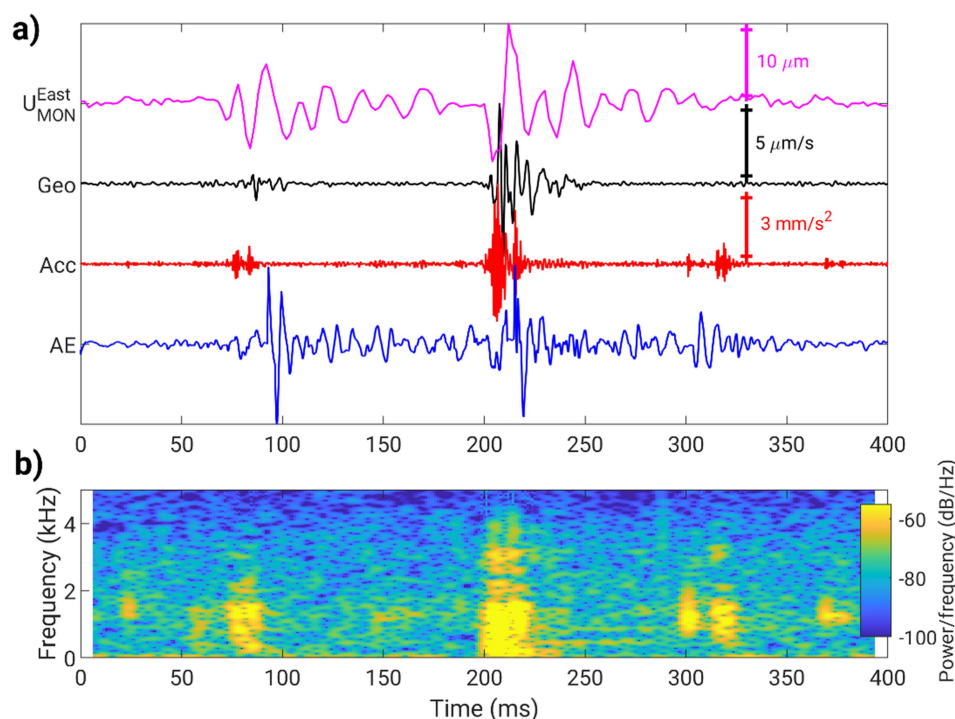


Figure 6. Events recorded between $t=343.1$ and 343.5 s (Fig. 4b) by the SIMFIP deformation probe in the monitoring borehole (U_{MON}^{East}), the upper geophone (Geo) and accelerometer (Acc) and an acoustic sensor (AE). Amplitude of the signals are indicated, except for the acoustic sensor (uncalibrated sensor). Signals are filtered in the 5-200 Hz, 80-500Hz, 200-2000 Hz and 80-8000 Hz, respectively. The lower panel shows the spectrogram of the upper accelerometer record.

ORIGINAL

The period with most of the micro-earthquakes starts by two seismic events, separated by 0.125 s, at $t \sim 343$ s (Fig. 4b and 6). The second event has the largest amplitude in this test, with a peak ground velocity of 6.1 $\mu\text{m/s}$ and 1.6 $\mu\text{m/s}$ on the upper and lower vertical geophones, and a peak ground acceleration is 21.8 mm/s^2 and 3.1 mm/s^2 on the upper and lower vertical component of accelerometers, respectively. Both events are recorded on all sensors, including on the monitoring probe, where dynamic signals are observed on top of a slow transient deformation of 14 μm (Fig. 4b), which may contain the coseismic slips and some additional deformation. An accurate event location is here not possible, but using P-wave polarization and arrival times (Fischer et al., 2008), these events seem to occur at close distance (0.5 to 3 m) north-west of the monitoring probe. Applying a Brune model (Brune, 1970) on both accelerometer data and integrated geophone (Supplementary Fig. S6), we find rough estimations of the corner frequency of ~ 220 Hz and of the magnitude of $M \sim 2.5$, which may correspond to a source size of ~ 1 m (De Barros et al., 2016). Only very limited fluid pressure drop is observed in the monitoring chamber when these two earthquakes occur. They are followed by several micro-earthquakes of much smaller amplitude. Their low amplitude and the impossibility to get an accurate location estimation prevent the estimation, even rough, of their magnitudes.

Two other seismic bursts of ~ 10 micro-earthquakes are shown in Fig. 4c (348-349.5s) and Fig. 4d (351.5-353.5s). While the first burst only contains micro-earthquakes, the sequence in Fig. 4d first shows tremor signatures with pressure drops, later followed by seismicity. Neither magnitudes nor localization can be estimated for these events, because of the low signal-to-noise ratio particularly on the lower geophone and accelerometer. These bursts share similar characteristics with the first sequence (Fig. 4b). First, in all cases, seismicity is not directly associated with a large pressure change, even if they follow a pressure drop while tremors in Fig. 4d occur. Secondly, all three sequences occur after an increase of deformation rate northward, consistent with the main slip propagation. The deformation then sharply changes direction, with a main southward direction. The first earthquake in each sequence, which is also the largest one in Fig 4d and 4e, occurs at this transition time (Fig. 4b, c, d). The deformation then takes a few seconds to recover its northward direction.

5. Discussion

The seismic responses to the injection presented here are diverse, as they can be either (1) totally aseismic, (2) with tremor signatures (emerging signals or seen through increasing noise amplitude), or (3) with bursts of micro-earthquakes. The first stage of injection into the shale fault is completely devoid of micro-earthquakes, although slip occurs, propagates and eventually creates a hydraulic connection from the injection chamber to the monitoring chamber, and beyond. A large component of the deformation is aseismic. This was similarly observed in other decameter-scale experiments performed in shale, using deformation measures, seismic-to-aseismic energy and seismic velocity variations (De Barros et al., 2019, 2016; Rivet et al., 2016), or above large-scale reservoirs (Bourouis and Bernard, 2007; Eyre et al., 2019; Wei et al., 2015). This aseismic slip induced by fluid is confirmed numerically by coupled hydro-mechanical experiments that aim at reproducing the monitoring data presented here (Cappa et al., 2022). However, a significant increase in the low frequency noise accompanies the fluid-driven slip propagation when reaching the monitoring point, in a period where no micro-earthquakes are detected (Fig. 2d and Supplementary Fig. S1-S3). Later, some tremor signals emerge above noise and are coupled to fluid pressure drops, such as during the main failure at the monitoring point. Toward the end of the injection, tremors alternate with small bursts of seismicity that are associated to fault movements but only loosely coupled to fluid pressure. This temporal sequence, starting from aseismic, to tremors and finally to micro-earthquakes, is similar to the seismic response of an injection experiment in more permeable limestone (Derode et al., 2015; Guglielmi et al., 2015a).

Micro-earthquakes occur as bursts of events, during episodes with very limited pressure changes, but with large deformation recorded on the monitoring probe. Thus, this deformation is not associated to any slip-induced dilatancy effects or tensile deformation, as they would have modified the pressure level. This is quite unlikely given the large opening component measured by both deformation probes during this injection test (Cappa et al., 2022; Guglielmi et al., 2020). Alternatively, micro-earthquakes may occur outside the fluid-invaded area, on structures that are not hydraulically connected to the injection. Moreover, they occur with a sudden change of deformation direction, from the North-West direction (main failure propagation direction) to the South. This confirms that these events do not likely occur on the main fluid-activated slipping patch. This was already observed in shale reservoirs (Eyre et al., 2019; Kettlety et al., 2020), and in-situ experiments (De Barros et al., 2018), where seismic

events can occur far from the injection location. Therefore, micro-earthquakes may not be a direct response to the fluid pressure perturbation, but only a by-product of the induced deformation. They may be triggered by the stress concentrations in response to the main propagating slip rather than by a decrease of the effective stress. Seismicity only occurs in a late phase of the experiment, which may suggest that a certain amount of accumulated deformation is needed over the fault zone to develop a stress perturbation strong enough to trigger seismic failures on fault segments away from the pressurized area. Moreover, shale is known to have rate-strengthening frictional properties (Kohli and Zoback, 2013), and seismicity may occur only when stress perturbations reach structures with rate-weakening properties (De Barros et al., 2016). Scaly clays in the main fault core at Mont Terri (Laurich et al., 2017) might be good candidates for that, as laboratory experiments on this material showed that they may allow earthquake triggering over short critical nucleation lengths (Orellana et al., 2018). When the main slipping plane gets closer to the main fault core in the second half of the test (Fig. 1a), it might critically perturb stress state on scaly clays, hence triggering seismic events.

Several possibilities may explain why the slip on the main injected faults, directly driven by fluid-pressure increase, do not occur as fast-slip earthquakes in this experiment. It might be because of (1) a general rate-strengthening frictional properties of the Mont-Terri shales (Orellana et al., 2018; ; Bigaroni et al, 2023), (2) a dilatant shear mechanism leading to an interplay between propagating slip and fluid diffusion (Scuderi and Collettini, 2018; Zoback et al., 2012), or (3) an increase of the earthquake nucleation length, inversely proportional to the fluid pressure increase, thus inhibiting seismic rupture in the pressurized area (Cappa et al., 2019). However, while the first part of the test is totally devoid of seismicity, an increase of noise amplitude is observed when the slip on the main injected faults approaches the monitoring probe. Even if we cannot characterize in detail this signature, it seems related to local transient effects and not to experimental noise. Qualitatively speaking, this long lasting, emergent signal might be similar to the tremors observed later in the sequence, even if its low amplitude makes it difficult to distinguish from the noise that covers it.

The other class of seismic signatures are tremor-type signals that emerge from the noise. As with the micro-earthquakes, they occur after the hydraulic connections between both chambers, when the pressure is high in the monitoring chambers. They are associated with large pressure drops and deformation in the direction of the main slip propagation (North-West). Therefore, they seem directly related to changes in the fluid pressure in geological features that are hydraulically connected to the

monitoring chamber, and thus to the injection. Contrary to micro-earthquakes, they are likely associated with the main slipping plane, in or at the edge of the fluid-pressurized area. Moreover, phases with tremor-like signals may initiate complex sequences with micro-earthquakes, as in Fig. 4d. Similarly, at a larger scale, the noise amplitude increase precedes all the micro-earthquake bursts. The propagated slip may perturb the stress state in the areas around it, which triggers seismic events. In this case, tremor signals may be seen as precursory signals of induced seismicity.

The waveforms and frequency contents of the tremor signatures, seen as emergent events or through noise variations, are very different among the different detected signals. Even if seismic attenuation may strongly distort these signals that are recorded by different sensor types, the strong differences may also suggest different source processes or source size. Given their short durations, they cannot be a signature of far-field road and rail traffic or regional earthquakes (Caffagni et al., 2015; Li et al., 2018; Zecevic et al., 2016). They might be directly a seismic signature of the slow-slip failures on the main injected faults, similarly to tremors recorded on subduction areas (Obara et al., 2004). This was hypothesized as the source process of tremor signals (LPLD) observed in shale reservoirs (Kumar et al., 2017; Zoback et al., 2012). They might originate from the slips of multiple asperities of small size, with a final spectral content modulated by comb effects (Dmitrieva et al., 2013). Alternatively, they may not be a direct signature of the deformation, but induced by the fluid flow through the resonance of fluid-filled fractures in response to pressure perturbation as the slip propagate or directly through the fluid turbulence itself (Hu et al., 2017; Julian, 1994; Tary et al., 2014). Here, the low number of sensors do not allow for a quantitative discrimination among these different processes. Finally, we cannot totally exclude that some or all tremors signatures originate from experimental noises (pump for example). In this case, the conclusions reach in this article stay valid, but the slip propagation on the main activated fault would be totally aseismic.

Tremor-like signatures have been observed in a similar experiment in limestone (Derode et al., 2015), above landslides, including in shale materials (Provost et al., 2018), and during some reservoir exploitation cases (Carr et al., 2017; Hu et al., 2017; Kumar et al., 2017). However, such observations are far from being ubiquitous. It might be due the difference in seismic responses among the different reservoir materials, fault networks and the evolution of physical properties of faults and fractures. Indeed, shale frictional properties may vary from rate strengthening, like in the Mont Terri Opalinus clay (Bigaroni et al., 2023), to rate weakening, mainly according to their clay and organic matter

contents (Kohli and Zoback, 2013). Relatively large seismic events have been triggered directly within shale reservoirs with rate-weakening frictional properties (Kettlety et al., 2020). The lack of observations of tremor-type signatures may be also due to the very low amplitude of such signals that make them buried in the noise. Adequate monitoring on reservoirs, with sensors in a very close vicinity of the injection, may then help to detect precisely weak signals that have not been widely observed.

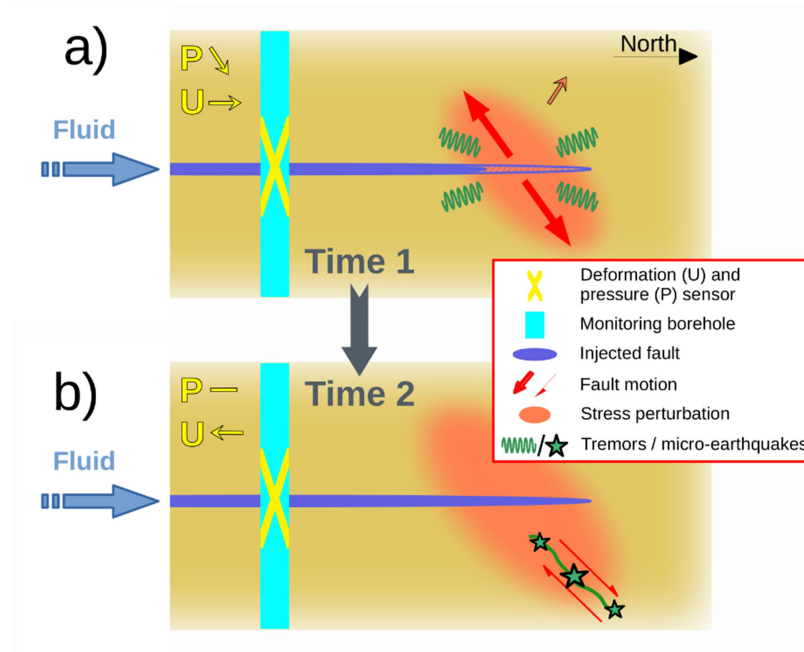


Figure 7. Conceptual sketch summarizing processes for tremors and micro-earthquakes. (a) At time 1, fluid-pressure directly drives the fault reactivation, with a tensile-shear mechanism, which is aseismic or triggers tremors seen as individual signals or noise variations. (b) This slip propagation perturbs the stress state, which then triggers micro-earthquakes on secondary faults away from the pressurized area at later time (time 2). Arrows following P and U sketch the observed variations of pressure and deformation, respectively.

In summary, we here identify two types of seismic signatures occurring in response to different hydro-mechanical processes at different times in the experiment. Figure 7 conceptually summarizes these dual behaviors. Tremor-like signatures, seen here either as emergent signals or as increase in the noise, seem directly related to the main fluid-driven slip propagation. This process may be totally aseismic, at least in the earlier phase. When propagating, the slip perturbs the stress state in the areas

around it, which then triggers seismic events on structures with adequate frictional properties away from the pressurized area. Therefore, tremor signals may be seen as precursory signals of triggered seismicity; they occur during the stress build-up phases that later leads to seismic failures. This can be seen on a short time-scale, with tremors signals coupled with pressure drops preceding a burst of seismic events (Fig. 4d). This succession is also observed at a much larger scale, as the noise amplitude increase corresponding to injection-driven slip propagation precedes all the seismic events.

This experiment occurs at shallow depth, hence in a low stress state environment, and the deforming area size is very limited (~10 m) in a strongly seismically attenuating medium. Therefore, the signals observed here are very small and the signal-to-noise ratio is low even on sensors close to the signal sources. Moreover, signals were not recorded by enough sensors to provide a quantitative analysis of their source properties as this experiment was designed as a preliminary test before an experiment with a denser seismic and strain monitoring network. We hope that the on-going injections in the Mont-Terri shale (Hopp et al., 2022), monitored by a dense network of accelerometer, Distributed Acoustic and Deformation Sensing (DAS and DDS) with optical fiber technology will allow to confirm the seismic signatures identified here and to shed new lights on their processes. Even with their limits, such experiments, where sensors are located close to the injected faults, allow the detection of weak signals and their empirical relation with the on-going processes during injection-induced fault slip. It is also worth noting that the dynamic signatures are seen on the SIMFIP probe when their frequency content are low enough. Therefore, with a higher sampling rate, the SIMFIP probes may be used as a joint seismometer and deformation sensor, which can prove very useful to better characterize earthquake source properties. Finally, as a large part of the deformation in shale formation may be aseismic, monitoring deformation is crucial to evaluate reservoir or caprocks mechanical responses to fluid injection. Remote observations from satellite geodesy (GPS or InSAR) are rare above reservoirs (Eyre et al., 2022; Pepin et al., 2022), and in most cases, deformation at the ground surface may be too small (< mm) to be measured precisely. This issue may be solved by installing deformation sensors, such as tiltmeters and strainmeters based on optical fiber DDS technology (Hopp et al., 2022) in boreholes close to the injection.

6. Conclusion

A fluid injection experiment was conducted at depth in a low permeability fault zone within the shale formation of the Mont Terri URL. The fluid-injected fault was reactivated and the slip propagated from the injection to a monitoring chamber, and beyond. We observed two different types of seismic signatures and associated them with two different hydromechanical processes. While tremor signals seem to be directly linked to the fluid-driven slip on the injected fault, micro-earthquakes occur later when stress perturbations from this main deformation are large enough to reach adequate geological asperities away from the pressurized area. Therefore, inferred tremor signals precede the triggered seismicity. They also are a more direct observation to monitor deformation and fluid flow in pressurized faults than micro-earthquakes. Their low amplitudes make them easily hidden in the noise at distances, but we show here that this issue may be tackled by characterizing the noise amplitude evolution. Therefore, monitoring the noise evolution with ultra-high resolution sensors spanning a broad band of frequencies at varying distances from the injection may bring additional insights into hydromechanical processes in poorly seismogenic shale materials, such as in sealing caprocks overlying subsurface reservoirs.

Acknowledgments

The Mt Terri experiment has been supported by the Federal Office of Topography (Swisstopo), Swiss Federal Nuclear Safety Inspectorate (ENSI), Japan Atomic Energy Agency (JAEA) and U.S. Department of Energy. Funding to LBNL's contributions to this study was provided by the Assistant Secretary for Nuclear Energy of the U.S. Department of Energy under Contract DEAC02-05CH11231. The analysis was partly supported by the ANR INSeis under contract ANR-22-CE49-0018. We thank the editor (Dr Sidao Ni) and two anonymous reviewers for their comments that helped improving the article.

Data Availability Statement

The raw data, including seismological, hydrological and mechanical data, of the injection test used in this study at Zenodo via [10.5281/zenodo.6811595](https://zenodo.org/record/6811595) with Creative Commons license (De Barros et al., 2022).

References

- Bigaroni, N., Scuderi M.M., Cappa F., Guglielmi Y., Nussbaum C., Aldega L., Pozzi G., Collettini C., 2023. Frictional properties of Opalinus Clay: influence of humidity, normal stress and grain size on frictional stability, *Geophysical J Int*, 233, 211-228, doi.org/10.1093/gji/ggac457
- Bourouis, S., Bernard, P., 2007. Evidence for coupled seismic and aseismic fault slip during water injection in the geothermal site of Soultz (France), and implications for seismogenic transients. *Geophys. J. Int.* 169, 723–732.
- Brune, J.N., 1970. Tectonic stress and the spectra of seismic shear waves from earthquakes. *J. Geophys. Res.* 75, 4997–5009.
- Caffagni, E., Eaton, D., van der Baan, M., Jones, J.P., 2015. Regional seismicity: A potential pitfall for identification of long-period long-duration events. *Geophysics* 80, A1–A5.
- Cappa, F., Guglielmi, Y., Nussbaum, C., De Barros, L., Birkholzer, J., 2022. Fluid migration in low-permeability faults driven by decoupling of fault slip and opening. *Nat. Geosci.* 15, 747–751. <https://doi.org/10.1038/s41561-022-00993-4>
- Cappa, F., Scuderi, M.M., Collettini, C., Guglielmi, Y., Avouac, J.-P., 2019. Stabilization of fault slip by fluid injection in the laboratory and in situ. *Sci. Adv.* 5, eaau4065. <https://doi.org/10.1126/sciadv.aau4065>
- Carr, T.R., Wilson, T., Kavousi, P., Amini, S., Sharma, S., Hewitt, J., Costello, I., Carney, B.J., Jordon, E., Yates, M., 2017. Insights from the Marcellus shale energy and environment laboratory (MSEEL), in: SPE/AAPG/SEG Unconventional Resources Technology Conference. OnePetro.
- Cornet, F.H., Helm, J., Poitrenaud, H., Etchecopar, A., 1998. Seismic and Aseismic Slips Induced by Large-scale Fluid Injections, in: Talebi, S. (Ed.), *Seismicity Associated with Mines, Reservoirs and Fluid Injections*, Pageoph Topical Volumes. Birkhäuser Basel, pp. 563–583.
- Das, I., Zoback, M.D., 2013. Long-period, long-duration seismic events during hydraulic stimulation of shale and tight-gas reservoirs—Part 1: Waveform characteristics. *Geophysics* 78, KS107–KS118.
- De Barros, L., Cappa, F., Guglielmi, Y., Duboeuf, L., Grasso, J.-R., 2019. Energy of injection-induced seismicity predicted from in-situ experiments. *Sci. Rep.* 9, 4999. <https://doi.org/10.1038/s41598-019-41306-x>
- De Barros, L., Daniel, G., Guglielmi, Y., Rivet, D., Caron, H., Payre, X., Bergery, G., Henry, P., Castilla, R., Dick, P., 2016. Fault structure, stress, or pressure control of the seismicity in shale? Insights from a controlled experiment of fluid-induced fault reactivation. *J. Geophys. Res. Solid Earth* 121, 4506–4522.
- De Barros, L., Guglielmi, Y., Cappa, F., Nussbaum, C., Birkholzer, J., 2022. Emerging tremors and increasing seismic noise precede micro-earthquakes triggered in a fluid-activated shale fault slip experiment (2015, Mt Terri URL, Switzerland) [Data set]. Zenodo. <https://doi.org/10.5281/zenodo.6811595>
- De Barros, L., Guglielmi, Y., Rivet, D., Cappa, F., Duboeuf, L., 2018. Seismicity and fault aseismic deformation caused by fluid injection in decametric in-situ experiments. *Comptes Rendus Geosci.* 350, 464–475. <https://doi.org/10.1016/j.crte.2018.08.002>
- Derode, B., Guglielmi, Y., De Barros, L., Cappa, F., 2015. Seismic responses to fluid pressure perturbations in a slipping fault. *Geophys. Res. Lett.* 42, 3197–3203.
- Dmitrieva, K., Hotovec-Ellis, A.J., Prejean, S., Dunham, E.M., 2013. Frictional-faulting model for harmonic tremor before Redoubt Volcano eruptions. *Nat. Geosci.* 6, 652.
- Eaton, D., van der Baan, M., Tary, J.-B., Birkelo, B., Spriggs, N., Cutten, S., Pike, K., 2013. Broadband microseismic observations from a Montney hydraulic fracture treatment, northeastern BC, Canada. *CSEG Rec.* 1150, 1250.
- Eyre, T.S., Eaton, D.W., Garagash, D.I., Zecevic, M., Venieri, M., Weir, R., Lawton, D.C., 2019. The role of aseismic slip in hydraulic fracturing–induced seismicity. *Sci. Adv.* 5, eaav7172. <https://doi.org/10.1126/sciadv.aav7172>

- Eyre, T.S., Samsonov, S., Feng, W., Kao, H., Eaton, D.W., 2022. InSAR data reveal that the largest hydraulic fracturing-induced earthquake in Canada, to date, is a slow-slip event. *Sci. Rep.* 12, 2043. <https://doi.org/10.1038/s41598-022-06129-3>
- Fang, Y., Elsworth, D., Wang, C., Ishibashi, T., Fitts, J.P., 2017. Frictional stability-permeability relationships for fractures in shales. *J. Geophys. Res. Solid Earth* 122, 1760–1776.
- Fischer, T., Hainzl, S., Eisner, L., Shapiro, S.A., Le Calvez, J., 2008. Microseismic signatures of hydraulic fracture growth in sediment formations: Observations and modeling. *J. Geophys. Res. Solid Earth* 113.
- Frank, W.B., 2016. Slow slip hidden in the noise: The intermittence of tectonic release. *Geophys. Res. Lett.* 43, 10,125-10,133. <https://doi.org/10.1002/2016GL069537>
- Gandossi, L., Von Estorff, U., 2013. An overview of hydraulic fracturing and other formation stimulation technologies for shale gas production. *Eur Commisison Jt Res Cent Tech Rep.* 26347.
- Guglielmi, Y., Birkholzer, J., Rutqvist, J., Jeanne, P., Nussbaum, C., 2017. Can Fault Leakage Occur Before or Without Reactivation? Results from an in Situ Fault Reactivation Experiment at Mont Terri. *Energy Procedia, 13th International Conference on Greenhouse Gas Control Technologies, GHGT-13*, 14–18 November 2016, Lausanne, Switzerland 114, 3167–3174. <https://doi.org/10.1016/j.egypro.2017.03.1445>
- Guglielmi, Y., Cappa, F., Avouac, J.-P., Henry, P., Elsworth, D., 2015a. Seismicity triggered by fluid injection–induced aseismic slip. *Science* 348, 1224–1226. <https://doi.org/10.1126/science.aab0476>
- Guglielmi, Y., Cappa, F., Lançon, H., Janowczyk, J.B., Rutqvist, J., Tsang, C.F., Wang, J.S.Y., 2014. ISRM Suggested Method for Step-Rate Injection Method for Fracture In-Situ Properties (SIMFIP): Using a 3-Components Borehole Deformation Sensor. *Rock Mech. Rock Eng.* 47, 303–311. <https://doi.org/10.1007/s00603-013-0517-1>
- Guglielmi, Y., Elsworth, D., Cappa, F., Henry, P., Gout, C., Dick, P., Durand, J., 2015b. In situ observations on the coupling between hydraulic diffusivity and displacements during fault reactivation in shales. *J. Geophys. Res. Solid Earth* 120, 7729–7748. <https://doi.org/10.1002/2015JB012158>
- Guglielmi, Y., Nussbaum, C., Cappa, F., De Barros, L., Rutqvist, J., Birkholzer, J., 2021. Field-scale fault reactivation experiments by fluid injection highlight aseismic leakage in caprock analogs: Implications for CO₂ sequestration. *Int. J. Greenh. Gas Control* 111, 103471. <https://doi.org/10.1016/j.ijggc.2021.103471>
- Guglielmi, Y., Nussbaum, C., Jeanne, P., Rutqvist, J., Cappa, F., Birkholzer, J., 2020. Complexity of Fault Rupture and Fluid Leakage in Shale: Insights From a Controlled Fault Activation Experiment. *J. Geophys. Res. Solid Earth* 125, e2019JB017781. <https://doi.org/10.1029/2019JB017781>
- Hopp, C., Guglielmi, Y., Rinaldi, A.P., Soom, F., Wenning, Q., Cook, P., Robertson, M., Kakurina, M., Zappone, A., 2022. The Effect of Fault Architecture on Slip Behavior in Shale Revealed by Distributed Fiber Optic Strain Sensing. *J. Geophys. Res. Solid Earth* 127, e2021JB022432. <https://doi.org/10.1029/2021JB022432>
- Hu, H., Li, A., Zavala-Torres, R., 2017. Long-period long-duration seismic events during hydraulic fracturing: Implications for tensile fracture development. *Geophys. Res. Lett.* 44, 4814–4819. <https://doi.org/10.1002/2017GL073582>
- Hulbert, C., Jolivet, R., Gardonio, B., Johnson, P.A., Ren, C.X., Rouet-Leduc, B., 2022. Tremor Waveform Extraction and Automatic Location With Neural Network Interpretation. *IEEE Trans. Geosci. Remote Sens.* 60, 1–9. <https://doi.org/10.1109/TGRS.2022.3156125>
- Jeanne, P., Guglielmi, Y., Rutqvist, J., Nussbaum, C., Birkholzer, J., 2018. Permeability Variations Associated With Fault Reactivation in a Claystone Formation Investigated by Field Experiments and Numerical Simulations. *J. Geophys. Res. Solid Earth* 123, 1694–1710. <https://doi.org/10.1002/2017JB015149>
- Julian, B.R., 1994. Volcanic tremor: Nonlinear excitation by fluid flow. *J. Geophys. Res. Solid Earth* 99, 11859–11877.
- Kettlety, T., Verdon, J.P., Werner, M.J., Kendall, J.M., 2020. Stress Transfer From Opening Hydraulic Fractures Controls the Distribution of Induced Seismicity. *J. Geophys. Res. Solid Earth* 125, e2019JB018794. <https://doi.org/10.1029/2019JB018794>

- Kohli, A.H., Zoback, M.D., 2013. Frictional properties of shale reservoir rocks. *J. Geophys. Res. Solid Earth* 118, 5109–5125.
- Kumar, A., Zorn, E., Hammack, R., Harbert, W., 2017. Long-period, long-duration seismicity observed during hydraulic fracturing of the Marcellus Shale in Greene County, Pennsylvania. *Lead. Edge* 36, 580–587.
- Laurich, B., Urai, J.L., Nussbaum, C., 2017. Microstructures and deformation mechanisms in Opalinus Clay: Insights from scaly clay from the Main Fault in the Mont Terri Rock Laboratory (CH). *Solid Earth* 8, 27–44.
- Li, C., Li, Z., Peng, Z., Zhang, C., Nakata, N., Sickbert, T., 2018. Long-Period Long-Duration Events Detected by the IRIS Community Wavefield Demonstration Experiment in Oklahoma: Tremor or Train Signals? *Seismol. Res. Lett.* 89, 1652–1659. <https://doi.org/10.1785/0220180081>
- Martin, C.D., Lanyon, G.W., 2003. Measurement of in-situ stress in weak rocks at Mont Terri Rock Laboratory, Switzerland. *Int. J. Rock Mech. Min. Sci.* 40, 1077–1088.
- Maxwell, S.C., Rutledge, J., Jones, R., Fehler, M., Duncan, P.M., Eisner, L., 2010. 10. Passive Seismic. *Geophys. Today*.
- Nussbaum, C., Bossart, P., Amann, F., Aubourg, C., 2011. Analysis of tectonic structures and excavation induced fractures in the Opalinus Clay, Mont Terri underground rock laboratory (Switzerland). *Swiss J. Geosci.* 104, 187–210.
- Obara, K., Hirose, H., Yamamizu, F., Kasahara, K., 2004. Episodic slow slip events accompanied by non-volcanic tremors in southwest Japan subduction zone. *Geophys. Res. Lett.* 31. <https://doi.org/10.1029/2004GL020848>
- Olabode, A., Bentley, L., Radonjic, M., 2012. Shale caprock integrity under carbon sequestration conditions, in: *AIP Conference Proceedings 4*. American Institute of Physics, pp. 347–352.
- Orellana, L.F., Scuderi, M.M., Collettini, C., Violay, M., 2018. Do scaly clays control seismicity on faulted shale rocks? *Earth Planet. Sci. Lett.* 488, 59–67. <https://doi.org/10.1016/j.epsl.2018.01.027>
- Pepin, K. S., Ellsworth, W. L., Sheng, Y., Zebker, H.A., 2022. Shallow aseismic slip in the Delaware Basin determined by Sentinel-1 InSAR. *Journal of Geophysical Research: Solid Earth*, 127, e2021JB023157. <https://doi.org/10.1029/2021JB023157>
- Provost, F., Malet, J.-P., Hibert, C., Helmstetter, A., Radiguet, M., Amitrano, D., Langet, N., Larose, E., Abancó, C., Hürlimann, M., Lebourg, T., Levy, C., Le Roy, G., Ulrich, P., Vidal, M., Vial, B., 2018. Towards a standard typology of endogenous landslide seismic sources. *Earth Surf. Dyn.* 6, 1059–1088. <https://doi.org/10.5194/esurf-6-1059-2018>
- Rivet, D., De Barros, L., Guglielmi, Y., Cappa, F., Castilla, R., & Henry, P. (2016). Seismic velocity changes associated with aseismic deformations of a fault stimulated by fluid injection. *Geophysical Research Letters*, 43(18), 9563-9572.
- Rouet-Leduc, B., Hulbert, C., Bolton, D.C., Ren, C.X., Riviere, J., Marone, C., Guyer, R.A., Johnson, P.A., 2018. Estimating fault friction from seismic signals in the laboratory. *Geophys. Res. Lett.* 45, 1321–1329.
- Sarout, J., Le Gonidec, Y., Ougier-Simonin, A., Schubnel, A., Guéguen, Y., Dewhurst, D.N., 2017. Laboratory micro-seismic signature of shear faulting and fault slip in shale. *Phys. Earth Planet. Inter.* 264, 47–62.
- Scuderi, M.M., Collettini, C., 2018. Fluid Injection and the Mechanics of Frictional Stability of Shale-Bearing Faults. *J. Geophys. Res. Solid Earth* 123, 8364–8384. <https://doi.org/10.1029/2018JB016084>
- Tary, J.-B., Van der Baan, M., Eaton, D.W., 2014. Interpretation of resonance frequencies recorded during hydraulic fracturing treatments. *J. Geophys. Res. Solid Earth* 119, 1295–1315.
- Thury, M., Bossart, P., 1999. The Mont Terri rock laboratory, a new international research project in a Mesozoic shale formation, in Switzerland. *Eng. Geol.* 52, 347–359.
- Trnkoczy, A., 2009. Understanding and parameter setting of STA/LTA trigger algorithm, in: *New Manual of Seismological Observatory Practice (NMSOP)*. Deutsches GeoForschungsZentrum GFZ, pp. 1–20.
- Wang, B., Kao, H., Yu, H., Visser, R., Venables, S., 2022. Physical factors controlling the diverse seismogenic behavior of fluid injections in Western Canada. *Earth Planet. Sci. Lett.* 589, 117555. <https://doi.org/10.1016/j.epsl.2022.117555>

- Wei, S., Avouac, J.-P., Hudnut, K.W., Donnellan, A., Parker, J.W., Graves, R.W., Helmberger, D., Fielding, E., Liu, Z., Cappa, F., 2015. The 2012 Brawley swarm triggered by injection-induced aseismic slip. *Earth Planet. Sci. Lett.* 422, 115–125.
- Zecevic, M., Daniel, G., Jurick, D., 2016. On the nature of long-period long-duration seismic events detected during hydraulic fracturing On the nature of LPLD events. *Geophysics* 81, KS113–KS121.
- Zoback, M.D., Kohli, A., Das, I., McClure, M., 2012. The importance of slow slip on faults during hydraulic fracturing stimulation of shale gas reservoirs, in: *SPE Americas Unconventional Resources Conference*. OnePetro.

ORIGINAL UNEDITED MANUSCRIPT